Temperature Treatment of Highly Porous Zirconium-Containing Metal-Organic Frameworks Extends Drug Delivery Release

Michelle H. Teplensky,[1] Marcus Fantham,[1] Peng Li,[2] Timothy C. Wang,[2] Joshua P. Mehta,[1,3] Laurence J. Young,[1] Peyman Z. Moghadam,[1] Joseph T. Hupp,[2] Omar K. Farha,[2,4] Clemens F. Kaminski,[1,] and David Fairen-Jimenez[1,*]*

[1]Department of Chemical Engineering and Biotechnology, University of Cambridge, UK

[2]Department of Chemistry, Northwestern University, Evanston, USA

[3]Department of Chemistry, University of Cambridge, UK

[4]Department of Chemistry, Faculty of Science, King Abdulaziz University, Jeddah 21589, Saudi Arabia

ABSTRACT

Utilizing metal-organic frameworks (MOFs) as a biological carrier can lower the amount of active pharmaceutical ingredient (API) required in cancer treatments to provide a more efficacious therapy. In this work, we have developed a temperature treatment process for delaying the release of a model drug compound from the pores of NU-1000 and NU-901, while

taking care to utilize these MOFs' large pore volume and size to achieve exceptional model drug loading percentages over 35 wt.%. Video-rate super-resolution microscopy reveals movement of MOF particles when located outside of the cell boundary, and their subsequent immobilization when taken up by the cell. Through the use of optical sectioning structured illumination microscopy (SIM), we have captured high-resolution 3D images showing MOF uptake by HeLa cells over a 24 h period. We found that addition of a model drug compound into the MOF and the subsequent temperature treatment process does not affect the rate of MOF uptake by the cell. Endocytosis analysis revealed that MOFs are internalized by active transport, and that inhibiting the *cavaeloe-mediate* pathway significantly reduced cellular uptake of MOFs. Encapsulation of an anticancer therapeutic, alpha-cyano-4-hydroxycinnamic acid (α-CHC), and subsequent temperature treatment produced loadings of up to 81 wt.% and demonstrated efficacy at killing cells beyond the *burst release effect*.

Introduction

Cancer is a major health problem worldwide. In 2012, there were more than 14 million cases of cancer diagnosed, and over the next two decades, this number is expected to grow by 70%.[1] In the United States of America, it is expected that 1 in 2.5 people will develop some form of cancer during their lifetime.[2] Patients diagnosed with cancer rely on active pharmaceutical ingredients (APIs) to eliminate the disease, reduce side effects, and prolong their lives. However, most APIs suffer from low stability, poor solubility, and an inability to bypass biological barriers.[3] One critical problem of compounds investigated in early-stage API development is that they present such short half-lives that are unsuitable for use as a pharmacological treatment, and therefore are not even worth funding through clinical trials.[4,5] Furthermore, current treatments are mostly untargeted and result in non-specific biodistribution, meaning that healthy cells are

killed as a negative side-effect of the treatment.[6] Additionally, the probability of patients following treatment through to completion is lower due to the undesirable side-effects, such as lower energy levels, as well as patients' previous health beliefs and attitudes, experiences with pharmacological therapies, and lack of overall motivation.[7] Therefore, the ability to implement a drug delivery system that could overcome inherent API limitations would provide a highly beneficial resource to pharmaceutical products and extend the capabilities of treatments currently in development.[8]

Different types of drug delivery systems are being researched to accomplish controlled, sustained release. To be effective, the system must: i) protect and target the APIs such that they reach their desired location, ii) last for extended periods of time to minimalize the discomfort and harmful side effects of systemic administration, and iii) ensure that the APIs are efficacious upon reaching their desired target.[3,9] The most common systems presently in use are organic, including lipids, hydrogels, micelles, and other forms of polymeric nanocarriers.[3,10–12] These systems have several shortcomings, including poor control of drug release and relatively low loading capacities: for example busulfan in liposome and polymer nanocarriers have loadings of only 5-6 wt.%.[13–15]

Metal-organic frameworks (MOFs), one of the most exciting developments in recent porous-materials science, are a class of porous hybrid self-assembling solids containing metal clusters connected by organic linkers. MOFs have been applied to catalysis,[16–19] gas storage and separation,[20–23] ion exchange,[24,25] and sensors[26,27] because of their potential for flexible rational design.[28] This has been exploited extensively to create structures of highly diverse composition (e.g. linkers varying from amines to polycarboxylates to imidazolates), shape (e.g. cubic, hexagonal, and prismatic geometries), and pore size (upwards of 6 nm).[3,29] Recently, MOFs have

emerged in the field of biomedicine.[3,30–32] They are of particular interest in biological delivery applications because of their highly tunable surface functionalities and ability to encapsulate high loadings of active molecules,[29,33] requiring less API to achieve the necessary pharmaceutical effect and overcoming the drawbacks of organic drug delivery systems. In addition, many MOFs are also confirmed to be non-toxic.[3,34] Recent advances in this area include the exploration of iron-based MOFs for delivery of anti-tumoral and anti-HIV drugs, and zirconium-based MOFs for co-delivery of cisplatin and pooled siRNAs.[33,35] In particular, the low stability of some MOFs in aqueous solvents can be seen as an advantage for drug delivery systems since their breakdown can prevent accumulation in the body, ensuring lower cytotoxicity.[36]

We have, among others, utilized Zr-based MOFs in the past because of their high level of biocompatibility and their relatively high mechanical, thermal, and chemical stability.[36–40] Some of these structures, particularly those with longer linkers, have attracted significant attention in the last years due to the possibility of developing mesoporosity while keeping an optimal stability.[41] In particular, NU-1000 and NU-901 are two MOFs formed by a parent-framework node of octahedral Zr_6-cluster capped by eight μ_3-OH ligands, where eight of the twelve edges are linked to TBAPy ligands (Supplementary Information, Figure S1). In NU-1000, the 3D structure can be described as 2D Kagome sheets stacked by TBAPy ligands;[41] from the N_2 adsorption isotherm at 77 K it presents a BET area of 2320 m^2g^{-1} and a total pore volume of 1.4 cm^3g^{-1} (Figure S2). In NU-901, the 3D structure can be described as stacked diamond-shaped channels;[42] from the N_2 adsorption isotherm at 77 K it presents a BET area of 2500 m^2g^{-1} and a total pore volume of 1.29 cm^3g^{-1} (Figure S2). The largest pore dimension for NU-1000 and NU-901, respectively, is 30 Å and 27 Å, creating large pore cavities that are advantageous for high

internal loading capacities. The thermal gravimetric analysis (TGAs) of these two Zr-based MOFs are shown in Figure S3, demonstrating their high thermal stability.

While NU-1000 and NU-901 are hypothesized to reach extremely high loading capacities due to their large pore volumes, there has been concern about the *burst release effect* – an undesirable phenomenon where most of the load escapes within a short time, causing potential toxicity and lower efficacy.[43] In previous works, we investigated the use of ball-milling to amorphisize a MOF as a way of entrapping a model drug to delay release.[36,37] In this work, we now present an improved method that can handle mechanically fragile payloads. We have developed a mild temperature treatment protocol that causes partial pore collapse of NU-1000 and NU-901, thus delaying the release of a model compound, calcein, as well as the anticancer therapeutic alpha-Cyano-4-hydroxycinnamic acid (α-CHC).

To better understand the release of MOF payload *in vitro*, we have utilized structured illumination microscopy (SIM) to visualize the interaction of MOFs with live cells at an unprecedented level of detail. SIM is a super-resolution microscopy technique that is able to capture images with a resolution of 100nm – twice the resolution of a conventional diffraction-limited instrument – and provide optical sectioning, which facilitates three-dimensional image reconstruction.[44] Furthermore, SIM can image faster than any other super-resolution microscopy technique,[45] at frame rates exceeding 10 Hz per color channel.[46,47] We believe this is the first study of MOFs to employ super-resolution microscopy, and the first to utilize optical sectioning SIM to observe any nanocarrier in 3D. Through this work, we show the potential of engineering an optimal MOF nanosystem capable of providing long-term controlled release, as well as super-resolution methods for verifying *in vitro* phenomena.

Results & Discussion

MOF loading and temperature treatment

Figure 1 shows the powder X-ray diffraction (PXRD) patterns of both NU-901 and NU-1000, demonstrating excellent agreement with the simulated patterns. We loaded calcein, a model compound, into both MOFs. Calcein is a good model drug candidate as it is hydrophilic and has minimal membrane permeability without a vehicle.[36] It is also similar in size to doxorubicin, a widely-used anticancer therapeutic. Furthermore, its intrinsic fluorescence allows for easy detection using microscopy. Post loading, the critical Bragg peaks were maintained, confirming the stability of the MOF structure (see Figure S4a for Pawley fitting of the PXRD patterns). These post-loading samples are referred to as cal@MOF. It is worth noting that the PXRD of calcein is amorphous (Figure S4b), and that the slight broadening of the peaks is most likely a result of the loading process, which takes place in aqueous solvent and leads to small levels of decrystallization of the MOF. After calcein loading, we used a temperature treatment process at 180℃ on loaded samples in order to induce partial collapse of the MOF porosity around calcein and entrap it within the structure. We hypothesize that this should lead to slower release and avoid the *burst release effect*. The temperature-treated samples are referred to as cal@t.t.MOF. After the temperature treatment protocol, the critical 2θ peaks of the PXRD patterns are significantly broader and peak intensity is noticeably decreased compared to those of the crystalline-loaded sample (cal@MOF). This is in contrast with previous mechanical amorphization work where the peaks have completely disappeared,[36] suggesting that, in our temperature-treated MOF, the long range order was not completely destroyed by the pore collapse.

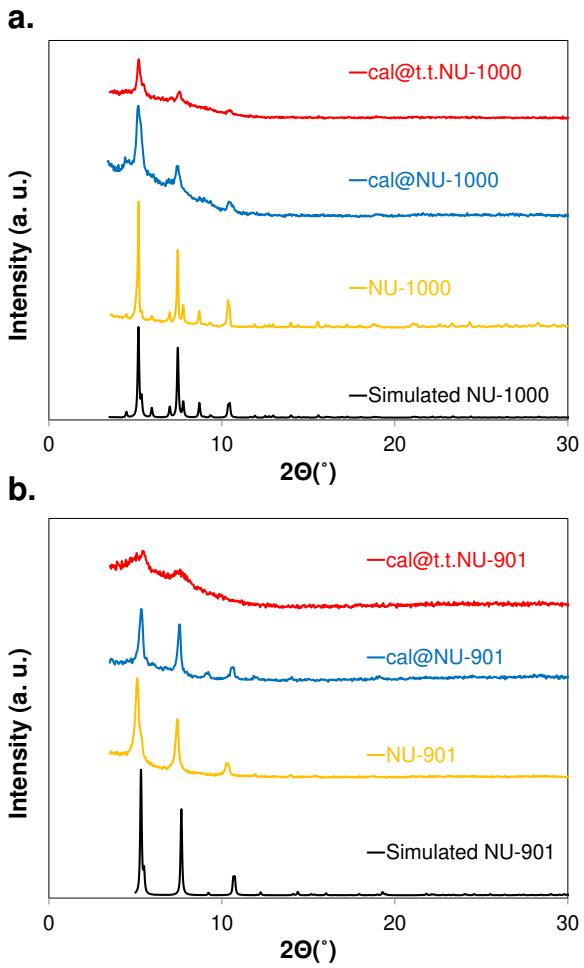

Figure 1. Powder X-ray diffraction (PXRD) patterns of **a**) synthesized NU-1000, cal@NU-1000, and cal@t.t.NU-1000 compared with the calculated one for NU-1000 and **b)** synthesized NU-901, cal@NU-901, and cal@t.t.NU-901 compared with the calculated one for NU-901.

To ensure calcein's stability during the temperature treatment process, NMR was run on digested loaded NU-901 samples pre and post treatment (Figure S5 and S6). The NMR-spectra reveals that the peaks attributed to calcein were not perturbed, suggesting no significant chemical changes to the model drug occur after heat treatment; analogous trends were observed with NU-1000. Additionally, the TGA for calcein (Figure S7) shows clearly that that any thermal degradation of the compound occurs at temperatures above 200°C, well above the treatment temperature.

Calcein-loaded NU-901 crystalline and temperature-treated samples had loadings of 37.0 ± 0.7 wt.% and 38.0 ± 0.2 wt.%, respectively. The loadings of the crystalline and temperature-treated NU-1000 samples, obtained through UV-Vis absorption measurement at 498 nm, were 41.6 ± 1.1 wt.% and 19.7 ± 0.4 wt.%, respectively. The loadings of these materials far exceeds the 5 wt.% loading of our previous work by mechanical amorphisation.[36] In order to prove that the loaded calcein is located in the internal porosity of the MOFs, we ran N_2 isotherms on calcein-loaded NU-1000 and NU-901 samples (Figure S8). We observed a substantial decrease in the BET area from 2320 m^2/g to 520 m^2/g for NU-1000 to cal@NU-1000, and from 2500 m^2/g to 200 m^2/g for NU-901 compared to cal@NU-901. Additionally, the shape of the isotherms was affected. As Figure S8a shows, the mesoporous step that occurs around relative pressure of 0.3 in NU-1000 has been shifted to a lower relative pressure in cal@NU-1000. We attribute this to calcein filling the inner walls of the mesoporous channels and allowing for complete adsorption of nitrogen in these channels at lower relative pressures. Furthermore, the relative intensity of the mesoporous step has decreased, which also suggests that calcein is loaded internally within the MOF. In Figure S8b, the small mesoporous step around 0.3 relative pressure has completely disappeared, which suggests that calcein has filled the MOF's porosity. Altogether, this demonstrates that calcein is adsorbed in the internal porosity in both MOFs.

From these loaded samples, we performed a release study in phosphate buffered saline (PBS) to evaluate the mass of calcein delivered. Figure 2 shows the release curves of calcein from both crystalline and temperature-treated samples, for both NU-1000 and NU-901. Although in the long-term the release profiles are similar, the critical first two days exhibit differences in the rate of calcein release between crystalline and temperature-treated samples for both NU-1000 and NU-901. The release profiles of t.t.NU-1000 show a delay of up to 7 days compared to the

crystalline NU-1000. In the first 4 hours they show a release of *ca.* 28 wt.% and 10 wt.% for NU-1000 and t.t.NU-1000, respectively (Figure 2a). These differences increase to 60 wt.% and 34 wt.% after 1 day; t.t.NU-1000 still retains slower release after 2 days, where crystalline sample calcein release is *ca.* 65 wt.% compared to *ca.* 44 wt.%. Complete release of calcein from both crystalline and temperature-treated samples of NU-1000 is not complete until about 7 weeks. The overlap of these two profiles does not occur until approximately 7 days. NU-901 shows similar release trends but the effect is not as pronounced as in the case with NU-1000 (Figure 2b). To further investigate this difference, we performed additional molecular mechanics calculations for both NU-901 and NU-1000, and calculated their mechanical properties. Interestingly, all primary mechanical properties such as bulk modulus, shear modulus and direction-dependent Young's moduli consistently show larger values for NU-901 suggesting a more robust structure (Table S1). We attribute the stronger framework integrity in NU-901 to the less dramatic effect of the temperature treatment. After the first 4 h, the crystalline form has released *ca.* 21 wt.% of its contents, compared with *ca.* 16 wt.% in t.t.NU-901. These differences increase to *ca.* 54 wt.% and *ca.* 47 wt.% after 1 day; t.t.NU-901 slightly delays the release of calcein up to 2 days before its profile crossed that of the crystalline sample. Complete release of calcein from both crystalline and temperature-treated samples of NU-901 is not complete until close to 3 weeks.

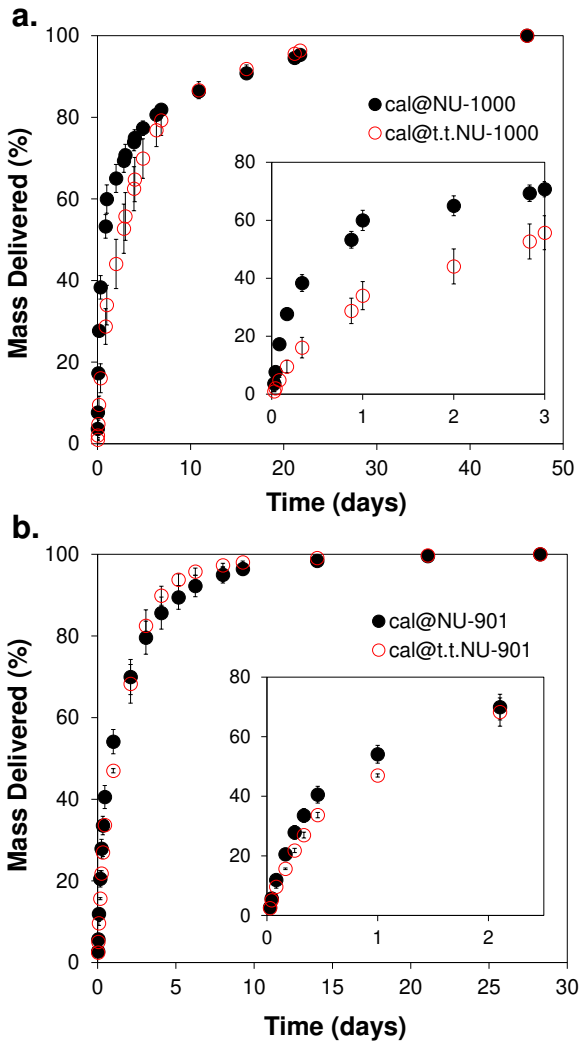

Figure 2. Calcein release from **a)** crystalline NU-1000 (black closed circles) and t.t.NU-1000 (red open circles), and **b)** crystalline NU-901 (black closed circles) and t.t.NU-901 (red open circles). Insets of both images show first few days of release study.

The crystalline release curves for both NU-901 and NU-1000 already show a substantial improvement on slowing the rate of release compared to previous studies of other crystalline MOFs.[13,30,48] In particular, Horcajada *et al.* showed that the complete release of the anticancer/antiviral drugs azidothymidine triphosphate, and cidofovir from crystalline MIL-100

occurred within 5 days and of doxorubicin in 12 days.[13] They also observed full release of ibuprofen within 3 and 6 days for MIL-100 and MIL-101, respectively.[30] We compared our release rates to UiO-66, another Zr-based MOF, where there is *ca.* 75 wt.% of calcein release from UiO-66 in just 6 hours.[36] This is much higher than the percentage released from our crystalline NU-901 or NU-1000 at 6 hours – *ca.* 28 wt.% and 33 wt.%, respectively. Overall, the temperature treatment slows down the early release of calcein from the two MOFs studies. The effect of this process is less dramatic than that of mechanical amorphization, which extends the release of calcein up to 30 days. However, this new mild treatment causes a collapse of porosity rather than an amorphization, and therefore is suitable for mechanically fragile payloads.

As our temperature-treatment process does not amorphisize the sample, we sought to determine if there was a morphological change in the material. Scanning electron microscopy (SEM) images in Figure 3 show the effect on morphology of various treatments during the loading and release process. The images of 150 nm NU-1000 prior to calcein loading (Figure 3a) and post-loading (Figure 3b) display no noticeable change in appearance compared with the temperature treated sample (Figure 3c). Figure 3d shows the MOF partway through the calcein release process. The morphology is significantly altered during the release process, which we attribute to degradation of the MOF by phosphate attack from PBS to the Zr-metal nodes.[3] The same trends were observed for NU-901 (Figure S9). We performed further analysis to understand the degradation of the MOFs in PBS (Figure S10).

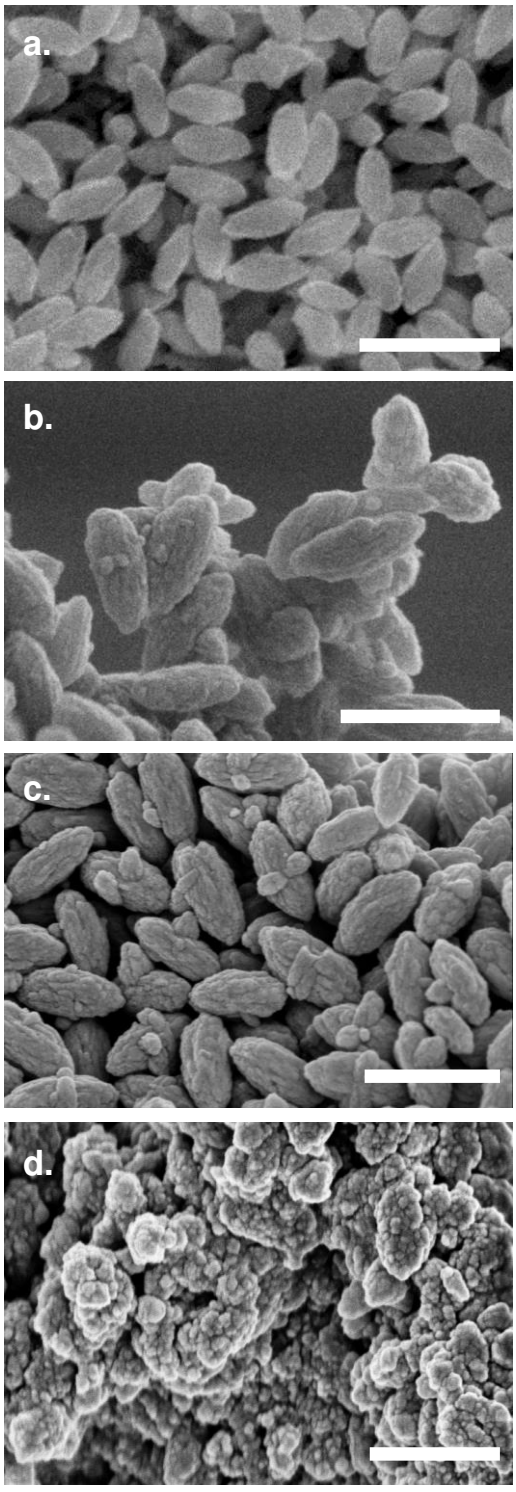

Figure 3. SEM Images of NU-1000 **a)** prior to calcein loading **b)** post-loading **c)** post-loading and temperature treatment and **d)** partway through calcein release process. Scale bars correspond to 400 nm.

Uptake of MOF by Hela cells

In order to visualize the interaction of MOFs with live cells we utilized structured illumination microscopy (SIM). A super-resolution SIM microscope is the ideal tool for visualizing our drug-delivery MOFs, since they have characteristic sizes at or below the 200 nm diffraction limit. Figures 4 and 5 show 3-color images of cells in the presence of 150 nm NU-1000 MOF, colored in green, with the nucleus colored in blue. Specific cellular vesicles are colored in magenta: in Figure 4, the magenta channel represents the lysosomes, whereas in Figure 5 it represents early endosomes. The lysosomes and endosomes in Figures 4 and 5, respectively, are stained to both help visualize cells and their intracellular organelle locations, and to show intracellular vesicles which could potentially contain MOF. These images show that the MOF has crossed the cell boundary, but it does not enter the nucleus. The cell visibly takes up NU-1000, as the magenta colored cellular organelles and green spots of MOF particles are in focus in the same plane.

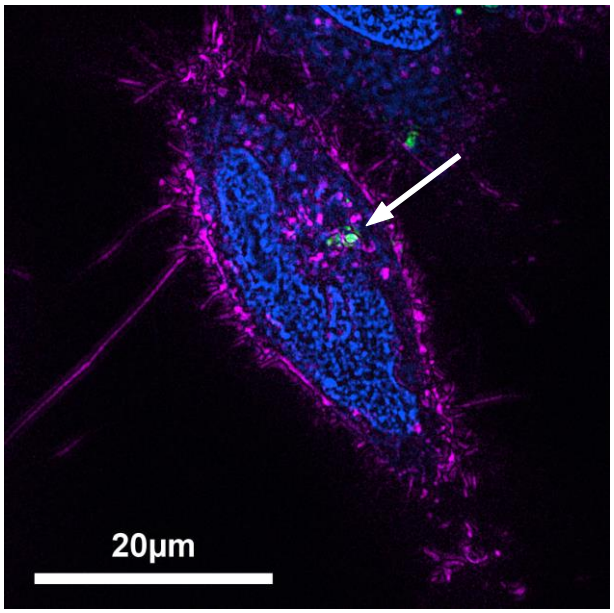

Figure 4. SIM 3-color image of HeLa cells demonstrating NU-1000 (150 nm) uptake into cellular boundary. Nucleus colored in blue, lysosomes colored in magenta, NU-1000 colored in green.

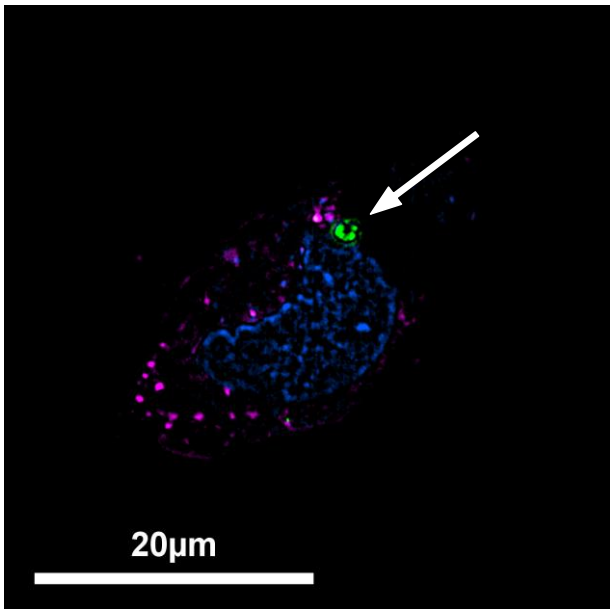

Figure 5. SIM 3-color image of HeLa cells demonstrating NU-1000 (150 nm) uptake into cellular boundary. Nucleus colored in blue, early endosomes colored in magenta, NU-1000 colored in green.

To provide more evidence of MOFs taken up by cells, we utilized the optical sectioning capabilities of SIM to reconstruct a 3D image (for an animation, please see Supporting Information, File 2) showing the MOF nanoparticles clearly within the boundaries of the cell. Figure 6 shows a single slice of the 3D reconstruction, displaying an ellipsoid of stained lysosomes in magenta and, in particular, one green dot representing fluorescent MOF that is co-located with the lysosome such that the color overlay has turned partially white. This verifies the internalization of the MOF within the cells. We conclude that cells can successfully take up the MOF nanoparticles and contain them inside the cell.

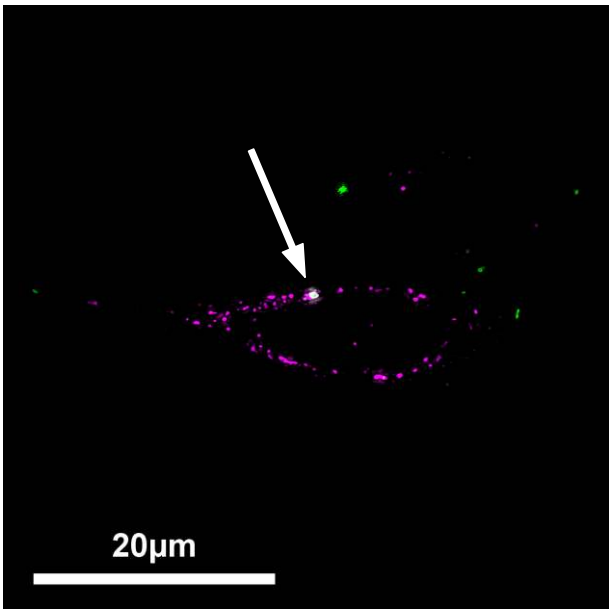

Figure 6. One slice of SIM 3D optical sectioning demonstrating NU-1000 (150 nm) internalization into HeLa cell, specifically bounded within cellular lysosome. Lysosomes colored in magenta, NU-1000 colored in green.

We exploited SIM's high-speed super-resolution imaging capability to compare the dynamics of MOFs in both inter- and extracellular space. A 2-color 60-second time lapse video (Supporting Information, File 3) shows the movement of NU-1000 MOF in 8× real time. MOFs in the extracellular space move much more rapidly than those located within the cell. This can be explained by the difference in the mediums between the extracellular and intercellular space, which are DMEM and cytoplasmic fluid, respectively. This adds more evidence that the MOF is taken up by the cell, and supports the hypothesis that the MOFs could be contained in an organelle or vesicle, further restricting intercellular movement.

In order to observe the uptake of our temperature-treated MOF by cells over an extended period of time, images of calcein-loaded temperature-treated NU-901 (cal@t.t.NU-901) with live HeLa cells were captured regularly over a period of 24 h, as shown in Figure 7. At t=0,

cal@t.t.NU-901 was added to a Lab-Tek well containing HeLa cells. Figure 7a shows that after 30 minutes of incubation, no MOF had entered the cells; however it can be seen gathering on the cell boundaries. After 1 hour (Figure 7b), there is evidence that the cell has internalized some MOF. Between 2 and 8 hours gradually more MOF gathers at the cell boundary and enters the cell (Figures 7c-e), and after 24 hours, Figure 7f shows that the cell has taken up a large amount of MOF. All datasets were captured in 3D and can be viewed interactively online at http://fpb.ceb.cam.ac.uk/MOF/.[49] Screenshots of the system in use for the 30 min and 24 h timepoints are shown in Figure 8. We hypothesized that the complexes situated around the cellular boundary will eventually be taken up through one of several potential endocytosis mechanisms, which could include active transport – clarithin-mediated endocytosis, caveolae-mediated endocytosis, micropinocytosis, or clarithin and caveolae-independent-mediated endocytosis – rather than passive transport.[50–53] Our experiments have shown that the uptake of MOF into the HeLa cells is not affected by the loading of the model drug calcein, nor by the temperature treatment process.

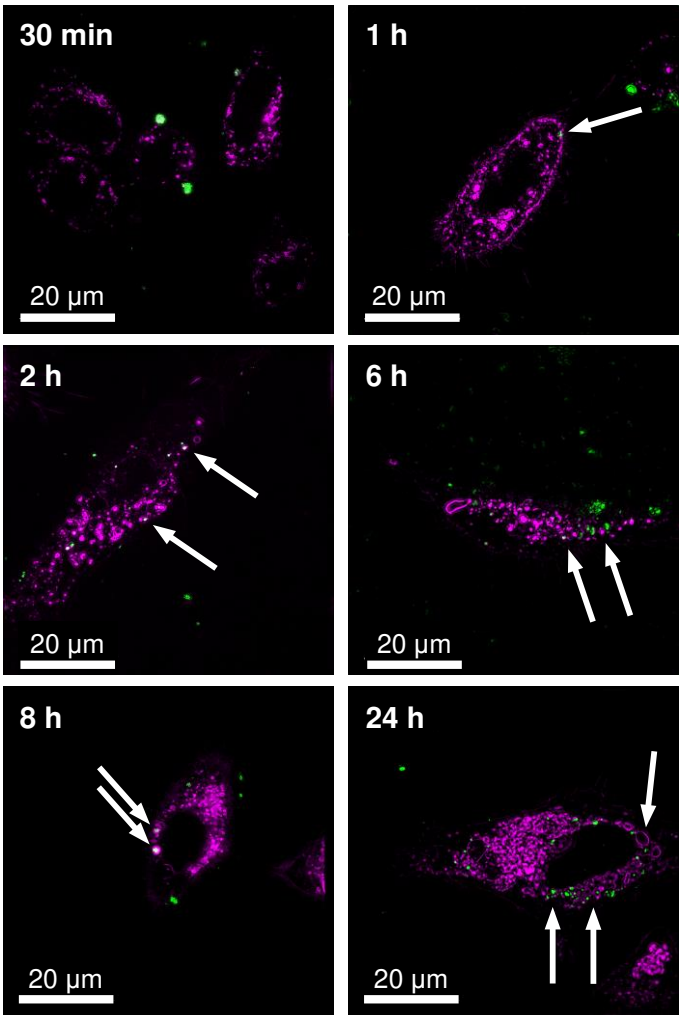

Figure 7 SIM images of HeLa cells incubated with calcein-loaded temperature-treated NU-901 (cal@t.t.NU-901) at 30 min, 1 h, 2 h, 6 h, 8 h and 24 h. Lysosomes colored in magenta, cal@t.t.NU-901 colored in green. These images are available at http://fpb.ceb.cam.ac.uk/MOF/ to view in interactive 3D.[49]

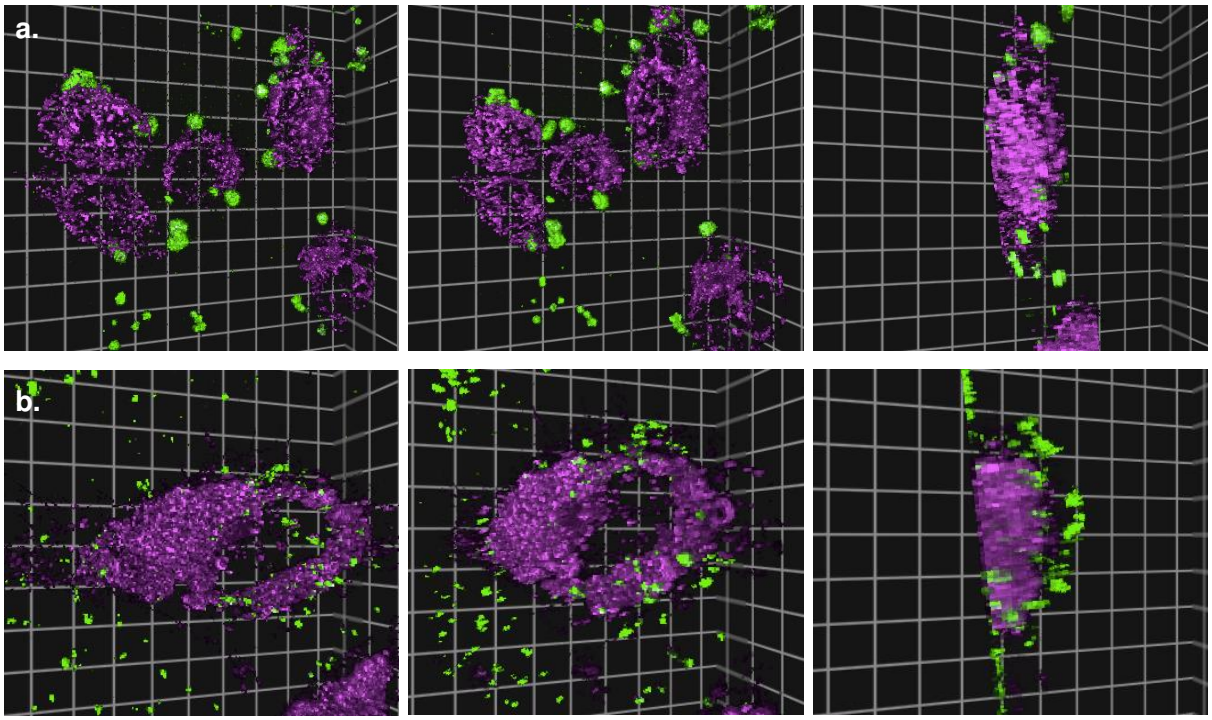

Figure 8. Screenshots of the interactive 3D system available at http://fpb.ceb.cam.ac.uk/MOF/.[49] HeLa cells incubated with calcein-loaded temperature-treated NU-901 (cal@t.t.NU-901) at **a)** 30 min and **c)** 24 h.

Endocytosis pathway studies

To test our hypothesis regarding the mechanisms by which the MOF complex is taken up by the HeLa cells, we performed studies to analyze uptake with the addition of endocytosis pharmacological inhibitors. HeLa cells were incubated with either cal@NU-1000 or cal@t.t.NU-901, the same two MOFs visualized with SIM. Figures 9 and 10 show the different levels of internal fluorescence, quantified by flow cytometry, in the presence of various pharmacological inhibitors. Sucrose and chlorpromazine are compounds which inhibit different stages of the *clathrin-mediated* endocytosis pathway. Sucrose inhibits endocytosis by trapping clathrin in microcages; chlorpromazine is believed to cause a loss of clathrin and the AP2 adaptor complex from the cell surface and artificial assembly on endosomal membranes.[54,55] Nystatin inhibits the

functioning of the *caveolae-mediated* endocytosis pathway by creating aggregates to accumulate cholesterol that sequesters the lipid from membrane structures.[55] The experiment was also run at 4°C without inhibitors to check that uptake was occurring through active – and not passive – transport, because at this temperature it is known that active processes are inhibited.[56]

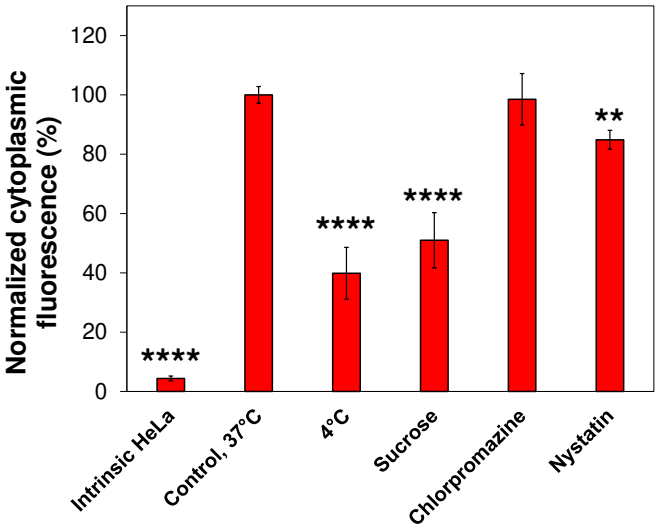

Figure 9. Effects of different inhibitors on the uptake of cal@NU-1000 into HeLa cells. All samples were measured through flow cytometry and run in minimum of triplicates. Statistical significance was calculated through one-way analysis of variance (one-way ANOVA) and a post Dunnett's Multiple Comparison Test compared to the Control, 37°C. (** $P<0.01$, **** $P<0.0001$)

The calcein in the samples, upon release inside the cell after successful MOF uptake, was quantified by flow cytometry and normalized to a control uptake of cal@NU-1000 run at 37°C. The intrinsic fluorescence of the HeLa cells was found to be negligibly low, such that any measurement of fluorescence could be assumed to come from the calcein inside the cells ($P<0.05$). Figure 9 shows that low temperature caused a significant decrease in cellular fluorescence, demonstrating that active transport is necessary for taking up MOF complexes into HeLa cells. Incubation with sucrose as an inhibitor showed a *ca.* 49% decrease in fluorescence, indicating that affecting this part of the *clathrin-mediated* pathway was enough to perturb

particle uptake. Nystatin as an inhibitor caused a decrease in fluorescence by *ca.* 15%, also demonstrating the importance of the *caveolae-mediated* pathway in the uptake of these particles.

Figure 10 shows the same endocytosis analysis using the cal@t.t.NU-901 particles as the nanocarrier. Again, the intrinsic fluorescence of HeLa cells was found to be negligibly low compared to calcein inside the cells ($P<0.05$). In low temperature conditions, the cell fluorescence was only *ca.* 42% of the control fluorescence, confirming the important role of active transport in internalizing MOFs. Incubation with sucrose showed no significant decrease in fluorescence, whereas incubation with chlorpromazine showed a *ca.* 16% decrease in fluorescence, indicating that for this MOF, a different part of the *clathrin-mediated* pathway was more important for particle uptake. We observe a decrease in fluorescence by *ca.* 33% when cells and cal@t.t.NU-901 are incubated with Nystatin, suggesting there is uptake occurring through the *caveolae-mediated* pathway.

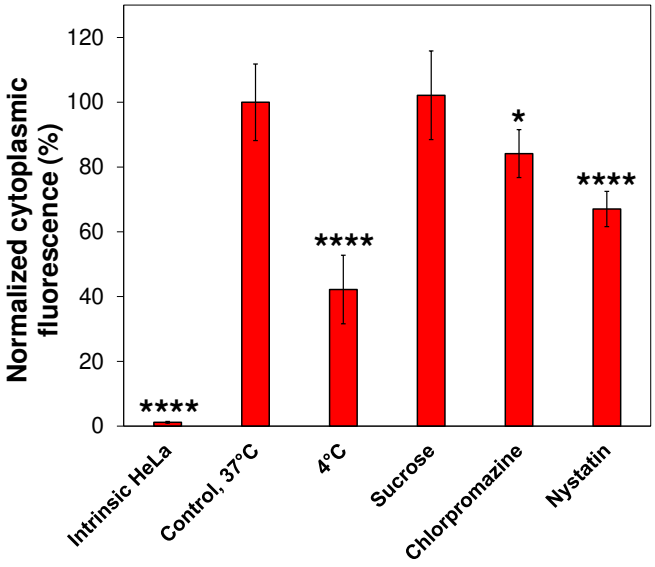

Figure 10. Effects of different inhibitors on the uptake of cal@t.t.NU-901 into HeLa cells. All samples were measured through flow cytometry and run in minimum of triplicates. Statistical significance was calculated through one-way analysis of variance (one-way ANOVA) and a post Dunnett's Multiple Comparison Test compared to Control, 37°C. (* $P<0.05$, **** $P<0.0001$)

Taken as a whole, the endocytosis study shows that uptake of MOFs by HeLa cells can occur through different active transport mechanisms, depending on the surface chemistry, charge, and size of the MOF complex. For both the MOFs tested in this work, the *caveolae-mediated* pathway plays a significant role in cellular uptake. This information could be used in future design of MOFs as nanocarriers to maximize the amount of MOF taken up by the cells, thus ensuring the most effective targeted delivery of the drug.

Therapeutic efficacy

Having confirmed by SIM that large proportions of MOF are taken up by the cells in just 8 hours, we altered the cargo loaded inside NU-901 and NU-1000 to deliver an anticancer therapeutic. The particular drug chosen was alpha-Cyano-4-hydroxycinnamic acid (α-CHC). This hydrophobic molecule has been suggested to prevent tumor growth because of its inhibition of monocarboxylate transporters (MCTs),[57,58] which promote migration and invasion processes in cancer.[59]

α-CHC was loaded into NU-901 (referred to as α-CHC@NU-901) and subsequently temperature treated (referred to α-CHC@t.t.NU-901) at 180 ℃, as described earlier. Ion-coupled plasma-optical emission spectroscopy (ICP-OES) was used to measure loadings of 54.6 wt.% and 79.0 wt.% for α-CHC@NU-901 and α-CHC@t.t.NU-901, respectively. The anticancer drug was also loaded into NU-1000 (referred to as α-CHC@NU-1000) and temperature treated (referred to as α-CHC@t.t.NU-1000) in the same manner, producing loadings of 68.5 wt.% and 81.0 wt.% for α-CHC@NU-1000 and α-CHC@t.t.NU-1000, respectively. TGA analysis showed that α-CHC does not degrade until *ca*. 230 ℃ (Figure S7), well above the 180 ℃ treatment

temperature, and should therefore retain its efficacy even when loaded into a temperature-treated MOF.

We assessed the drug efficacy using a metabolic activity assay, where a lower value of cell viability indicates a greater efficacy of the drug. We measured the viability of cells in the presence of α-CHC on its own as a control (free drug), and with α-CHC loaded into both crystalline and temperature-treated MOF, to quantify the effectiveness of these MOFs at delivering the drug to cells. For the studies, set concentrations of loaded MOF were added to the solution, and the relative drug concentration was calculated based on the ICP loading measurements. Figure 11 shows the cell viability for α-CHC@NU-1000 and α-CHC@t.t.NU-1000 after incubation for 8 h (Figure 11a) and 48 h (Figure 11b), as an indicator of drug efficacy. After just 8 hours, there is no significant difference in the efficacy between the crystalline and temperature-treated NU-1000. However, both profiles do indicate an efficacy that the free drug cannot achieve at 8 h, especially at drug concentrations above 0.5 mg/mL. Above this drug concentration, the MOF profiles show significant decline in cellular viability down to a final value of *ca.* 55% and *ca.* 44% viability for the highest tested drug concentration in α-CHC@NU-1000 and α-CHC@t.t.NU-1000, respectively. Compared to the cellular viability of the free drug control, which stays at *ca.* 100% for all tested drug concentrations at 8 h, using NU-1000 to deliver α-CHC provides a more effective drug delivery.

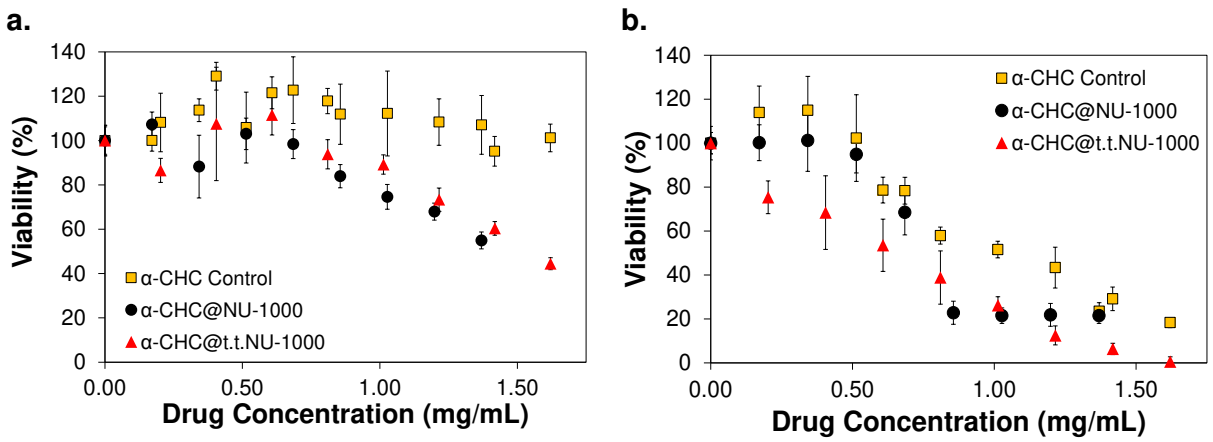

Figure 11. MTS Assays measuring enzymatic metabolic activity for α-CHC-loaded NU-1000 in both crystalline and temperature treated complexes for **a)** 8 h and **b)** 48 h of *in vitro* incubation. The free drug, α-CHC Control, is shown incubated for both time points in yellow. Samples were run in minimum of four replicates. Standard errors are shown for each given concentration.

After 48 h of incubation we observe a greater difference between the crystalline and temperature-treated NU-1000 profiles (Figure 11b). The temperature-treated sample showed an effect on cell viability even at the lowest tested drug concentration (0.2 mg/mL). As concentration is increased, the decline in cell viability continues steadily until no cells were detected as viable at a drug concentration of *ca.* 1.6 mg/mL. In contrast, the α-CHC@NU-1000 did not cause a significant change in cell viability until *ca.* 0.7 mg/mL of drug concentration, showing a similar trend to the free drug control. There is no significant change in the crystalline profile for viability compared with the control until a drug concentration of 0.85 mg/mL, where the viability drops to *ca.* 20% and maintains this efficacy for all higher concentrations. We hypothesize that the difference between the crystalline and temperature-treated samples is because the crystalline sample had already released a significant amount of payload before entering the cell, and therefore this free drug is in the solution and does not enter the cell within the MOF. It is only at higher concentrations where there is more drug still left in the crystalline

framework – even after this *burst release effect* – where the drug can be effective at killing the cells. In contrast, the temperature-treated MOF inhibits the *burst release effect,* and therefore still retains much of its drug loading within the 48 h incubation time. Thus, when the cell takes up these particles, there is still a high payload delivery, and therefore a greater effect on cell viability.

These same trends are observed in the 11 h (Figure 12a) and 48 h (Figure 12b) time points of the α-CHC@NU-901 and α-CHC@t.t.NU-901 *in vitro* studies. There is negligible difference between the effect of the crystalline and temperature-treated α-CHC-loaded MOF for the entirety of the drug concentration range tested after 11 h of incubation. However, both profiles do indicate significant efficacy compared to the free drug at concentrations higher than 0.4 mg/mL. The highest tested drug concentration in α-CHC@NU-901 and α-CHC@t.t.NU-901 (1.1 mg/mL and 1.6 mg/mL, respectively) yields cellular viability at *ca.* 30% after 11 hours.

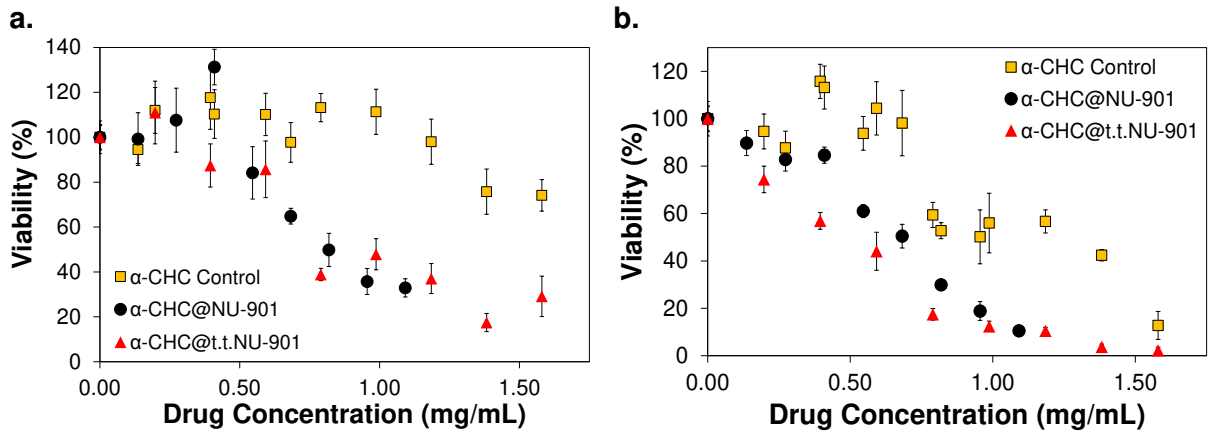

Figure 12. MTS Assays measuring enzymatic metabolic activity for α-CHC-loaded NU-901 in both crystalline and temperature treated complexes for a) 11 h and b) 48 h of *in vitro* incubation. The free drug control, α-CHC, is shown incubated for both time points in yellow. Samples were run in minimum of four replicates. Standard errors are shown for each given concentration.

After 48 h of incubation (Figure 12b), there is again a difference in the efficacy of crystalline versus temperature-treated MOFs. However, as also observed in the calcein release study (Figure 2), the differences were less dramatic for NU-901 than NU-1000. Both the crystalline and temperature-treated samples showed a slight decline in cell viability at the lowest drug concentrations compared to the control. For drug concentrations up to 1 mg/mL, the anticancer drug shows better efficacy when loaded into the temperature-treated MOF. We attribute this to the same reasoning regarding suppression of the *burst release effect* that applied to α-CHC@t.tNU-1000.

Conclusions

We have successfully developed an optimized protocol of treatment to delay the release of a model drug, calcein, from two Zr-based metal-organic frameworks, NU-1000 and NU-901. We utilized the surface tension of remaining aqueous solvent to collapse porosity when increasing the temperature, trapping the calcein within the framework. PXRDs of the temperature-treated MOF show lower peak intensity and peak broadening, which suggest partial degradation of the samples and decrease of crystallinity; however no morphological change can be seen on SEM images post-temperature treatment. Temperature treatment of MOFs with calcein loadings of over 35 wt.% can delay release of their payload compared to their crystalline forms by *ca.* 2-7 days; complete release is not seen until *ca.* 30-49 days. We applied, for the first time, structured illumination microscopy (SIM) - a super-resolution microscopy technique - in order to visualize MOF uptake into HeLa cells. We can confirm intracellular presence through 3D optical sectioning and reconstruction, and time lapses evaluating dynamics of movement of particles intra- and extracellularly. Experiments with endocytosis inhibitors reveal that the MOF is taken up by the cells through active transport, although the exact endocytosis pathway depends on the

surface chemistry and other factors of the MOF. For both NU-1000 and NU-901, cellular uptake was reduced when the *caveolae-mediate* pathway was inhibited. Finally, we loaded the MOFs with the pharmacologically relevant anticancer drug α-CHC to show that efficacy is improved using temperature-treated MOFs as a drug delivery system, reaching loadings of up to 81 wt.%.

Materials & Methods

Materials

NU-1000 (5 μm and 150 nm sizes), NU-901 (200 nm size), and their respective linker, H_4TBAPy, was obtained via synthesis. Calcein disodium salt was purchased from Sigma-Aldrich (UK, 21030-5G-F). HeLa cells were obtained from the ATCC and cultured with Dulbecco's modified Eagle's medium (DMEM, Sigma Aldrich D5671), fetal bovine serum (FBS, Sigma Aldrich F9665), 100x 200 mM L-glutamine (Life Technologies 25030024), and penicillin and streptomycin (P-S, Life Technologies 15140122). Phosphate-Buffered Saline (PBS, Sigma D8537) and 1x trypsin–EDTA (Life Technologies 25300054) were purchased. Trypan blue, was purchased from Thermo Fisher (UK, 15250061). Stains for lysosomes, CellLight® Lysosomes-RFP BacMam 2.0, early endosomes, CellLight® Early Endosomes-RFP BacMam 2.0, and nucleus, HCS NuclearMask™ Deep Red Stain (250X Concentrate in DMSO), were obtained from Thermo Fisher (UK, C10504, C10587, and H10294, respectively). Chlorpromazine hydrochloride (≥98%), Sucrose (≥99.5%), nystatin, and α-Cyano-4-hydroxycinnamic acid (≥98%, TLC, powder) was purchased from Sigma-Aldrich (UK). The CellTiter 96® AQueous Non-Radioactive Cell Proliferation Assay (MTS) was purchased from Promega (UK, G5421). All chemicals and biochemicals used were of analytical grade.

Synthesis

NU-1000 (Figure S1) was produced through previously published protocols,[60,61] which additionally describes the synthesis of the linker H_4TBAPy.[41,60] 5 μm-sized NU-1000 involved mixing $ZrOCl_2 \cdot 8H_2O$ (388 mg, 1.20 mmol) and benzoic acid (10.8 g, 88.4 mmol) in DMF (32 mL) and ultrasonically dissolving the mixture. The clear solution was incubated in an oven at 80˚C for 1 h, and allowed to cool to room temperature. H_4TBAPy (160 mg, 0.24 mmol) was added to this solution; the mixture was sonicated for 20 min. The yellow suspension was heated in an oven at 100˚C for 15.5 h and then allowed to cool to room temperature. The resulting material was isolated by centrifugation (7,750g for 5 min) and washed with DMF, activated with HCl (2 ml, 8 M solution), and subsequently washed with DMF again and acetone.

For nano-sized (150 nm) NU-1000, 1 mL of 970 mg (3.00 mmol) of $ZrOCl_2 \cdot 8H_2O$ and 16.0 g (131 mmol) of benzoic acid already dissolved in 80 mL of DMF in a 100 °C oven – was added to 1 mL of 200 mg (0.300 mmol) of the ligand dissolved in 80 mL of DMF in a 100°C oven. The mixture contained 20 μL trifluoroacetic acid (0.26 mmol). The entire vial was then placed into an oven at 100°C for 1 h, and after cooling to room temperature, the suspension was isolated by centrifugation at 7800 rpm for 10 min. The sample was washed once with DMF, twice with acetone, and activated with HCl.

To synthesize 200 nm NU-901, $ZrOCl_2$ (97 mg) and para-aminobenzoic acid (1.5 g) were added into a 6-dram vial with 10mL of DMF. The solution was incubated at 80°C for 1 hour, and then allowed to cool to room temperature. H_4TBAPy (40 mg) was added, and the mixture was heated at 100°C overnight. The resulting solid was separated by centrifugation, and extensively washed with DMF. The acid-activation with HCl (8 M, 0.5 mL) was performed with the sample suspended in DMF (13 mL). The vial was heated at 100 °C overnight and then was washed with

DMF before the solvent exchange with acetone. An N_2 isotherm was performed after sample activation at 120 °C overnight.

All MOFs were heat treated overnight, prior to experimental use, at 70°C in a vacuum oven overnight to remove any residue solvent.

Characterization of Crystallinity

Room temperature powder XRD (PXRD) was performed on both NU-901 and NU-1000 loaded and unloaded samples using a Bruker-D8 theta/theta machine with CuKα1 (λ = 1.5405 Å) radiation and a LynxEye position sensitive detector in Bragg Brentano parafocusing geometry. 2θ steps ranged from 2˚ to 50˚.

Characterization of Porosity

Characterization through N_2 adsorption was measured on either a TriStar II or 3Flex (Micromeritics) machine. For samples run on TriStar II, activation occurred in a sorption tube at 120 °C for 12 h under vacuum on a SmartVacPrep (Micromeritics). For the samples run on 3Flex, degassing occurring at 120 °C for 10 h. The nitrogen isotherm was measured from P/P_0 = 0 to 0.99 at 77 K (held by liquid nitrogen bath).

Thermogravimetry

Thermogravimetric analysis (TGA) was performed using a Perkin Elmer Pyris 1 thermal gravimetric analyzer, with the sample (*ca.* 1 mg) held on a platinum pan under a continuous flow of 20 mL/min N_2 gas. TGA curves were obtained using a heating rate of 5 °C/min and measuring from 100 to 600 °C.

Loading into MOFs

To load calcein in the MOFs, 10 mg of either NU-1000 or NU-901 was soaked in a 10 mg/mL calcein in diH_2O solution for 3 days in a 37℃ shaking incubator. After this initial load period,

the contents were centrifuged at 5400 g for 20-30 min and the supernatant was removed. The crystalline samples were then dried at 37℃ for 24 h. For the temperature treatment process, the samples were loaded into a high temperature vacuum oven at 180℃ for 24 h before use in drug release studies. To load α-CHC in the MOFs, 10 mg of either NU-1000 or NU-901 was soaked in a 5 mg/mL α-CHC in diH_2O solution for 3 days in a 37℃ shaking incubator. The same post-loading centrifugation and drying occurred for crystalline and temperature-treated samples as described above. All samples were washed once in PBS to remove any externally located payload.

Release Study

Release experiments were conducted over seven weeks at 37℃ in a shaking incubator. Samples of calcein-loaded MOF, in both crystalline and temperature-treated states, were loaded into 1.5 mL Eppendorf tubes with 1 mL 1X PBS. At each time point, samples were removed from the 37℃ shaking incubator, centrifuged at 16000 × g for 50 s, and the supernatant was collected for UV-Vis absorbance measurement at 498 nm. The removed supernatant in the Eppendorf tubes was replaced with 1 mL fresh 1X PBS, and the samples were placed back into the shaking incubator at 37℃ until the following time point.

Cell Culture

HeLa cells were maintained at 37°C and 5% CO_2 in high rich glucose (4500 mg/L) DMEM supplemented with 10% (v/v) FBS, 2 mM L-glutamine, 100 units/mL penicillin and 100 μg/mL streptomycin. The cells were passaged three times a week (at about 80% confluency) at a density of 2.8 x 10^6 cell/cm^2.

Cellular Uptake prior to SIM

Cells were cultured before being seeded at a density of 50,000-75,000 on an 8-well Lab-Tek II Chambered Coverglass (ThermoFisher 155409) for approximately 8-12 hours. Cells were then incubated with either BacMam Lysosome Stain or BacMam Early Endosome Stain (depending on the experiment) overnight at a particles-per-cell (PPC) of 20-30. The following day, the entire well contents were removed and washed once with 1X PBS before incubation with 200 μL of 0.3 mg/mL of MOF (150 nm NU-1000 or 200 nm cal@t.t.NU-901). After 4 hours, this solution was removed and washed once with 1x PBS, once with trypan blue, twice more with 1x PBS and then replaced with 200 μL of complete DMEM without phenol red. In experiments utilizing 3 color SIM, nuclear stain was added prior to the trypan blue wash and allowed to incubate for 30 min prior to removing and completing the remaining wash steps. For experiments using loaded MOF (cal@t.t.NU-901), time of incubation was specified as shown in SIM images; the subsequent wash steps were identical.

SIM Imaging

Images of the samples were collected using a custom built 3-color Structured Illumination Microscopy (SIM) setup which we have previously described.[46] A 60X/1.2NA water immersion lens (UPLSAPO 60XW, Olympus) focused the structured illumination pattern onto the sample. This lens also captured the samples' fluorescence emission light before imaging onto an sCMOS camera (C11440, Hamamatsu). Laser excitation wavelengths used were 488 nm (iBEAM-SMART-488, Toptica), 561 nm (OBIS 561, Coherent), and 640 nm (MLD 640, Cobolt), to excite fluorescence emission of MOF, lysosomes or endosomes, and DNA, respectively. Images were acquired using custom SIM software previously published.[46] Nine raw images were collected at each plane and recombined using a custom implementation of a Super-Resolution Optical Sectioning reconstruction algorithm.[47]

Endocytosis Experiments

HeLa cells were cultured before being seeded on a 24-well plate at a density of 100,000 cells/well for approximately 24 hours. Cells were then washed once with 1x PBS before a pre-treatment 30 min incubation with different inhibitors or conditions: sucrose (150 μL, 0.3 M), chlorpromazine (150 μL, 100 μM), nystatin (150 μL, 0.250 mg/mL) all at 37˚C and untreated cells at 4˚C. After the 30 min pre-treatment with inhibitory conditions, the media was entirely removed and replaced with a solution of 0.5 mg MOF in each conditions (sucrose (150 μL, 0.3 M), chlorpromazine (150 μL, 100 μM), nystatin (150 μL, 0.250 mg/mL), 4˚C media). The solution was incubated for 1.5 h at 37˚C, except for the condition incubated at 4˚C. After incubation, the well contents were removed and washed once with 1X PBS, once with trypan blue, twice more with 1x PBS, and then incubated for 5 min at 37˚C with trypsin. Fresh complete DMEM without phenol red was added to the wells after incubation and then contents were transferred to Eppendorf tubes and centrifuged at 1200 rpm for 5 min. The cells were re-suspended in 200μL complete DMEM without phenol red. Samples were kept on ice until measurement on a Cytek DxP8 analyzer cytometer. Analysis was completed with FlowJo and Prism software.

Cytotoxicity Analysis with Anticancer Drug

HeLa cells were cultured before being seeded on a 96-well plate at a density of 7500 cells/well for approximately 24 hours. The compounds being tested (α-CHC loaded MOFs and the α-CHC free drug) were dissolved in complete DMEM at different concentrations. Cells were then washed once with 1x PBS before incubation at 37˚C/5% CO_2 with the different concentrations of compounds for either 8, 11, or 48 h. After incubation, the well contents were removed and washed three to four times with 1X PBS. A solution of 100 μL of complete DMEM and 20 μL

MTS/phenazine methosulfate (20:1 ratio) was added to the wells and the contents were incubated for 1.5 h at 37˚C/5% CO_2. The plates were read by a SPECTROstar Nano at 490 nm.

ASSOCIATED CONTENT

Supporting Information.

The following files are available free of charge:

Supporting File #1. Structure of NU-1000 and NU-901, N_2 adsorption isotherms at 77 K, and thermogravimetry curves under N_2 atmosphere.

Supporting File #2 (3Drotation_nNU1000 in HeLa cell): We reconstructed a 3D image using the optical sectioning capabilities of SIM showing a HeLa cell with NU-1000 located within its boundaries (file type: .qt).

Supporting File #3 (Widefield Timelapse 2-color With Timestamp Faster-1_witharrow): We compared the dynamics of MOFs in both inter- and extracellular space with this 2-color 60-second time lapse video showing the movement of NU-1000 in 8× real time (file type: .qt).

AUTHOR INFORMATION

Corresponding Author

*df334@cam.ac.uk and *cfk23@cam.ac.uk

ACKNOWLEDGMENTS

M.T. thanks the Gates Cambridge Trust for funding, and S. Haddad and C. Hockings for helpful discussion. D.F.-J. thanks the Royal Society for funding through a University Research

Fellowship. O.K.F. and J.T.H. gratefully acknowledge DTRA for financial support (grant HDTRA-1-14-1-0014).

REFERENCES

(1) *World Cancer Report 2014*; Stewart, B. W.; Wild, C. P., Eds.; International Agency for Research on Cancer: Lyon, France, 2014.

(2) National Cancer Institute. Cancer Statistics https://www.cancer.gov/about-cancer/understanding/statistics (accessed Oct 20, 2016).

(3) Horcajada, P.; Gref, R.; Baati, T.; Allan, P. K.; Maurin, G.; Couvreur, P.; Férey, G.; Morris, R. E.; Serre, C. *Chem. Rev.* **2012**, *112*, 1232–1268.

(4) Lammers, T.; Subr, V.; Ulbrich, K.; Hennink, W. E.; Storm, G.; Kiessling, F. *Nano Today* **2010**, *5*, 197–212.

(5) Huang, X.; Brazel, C. S. *J. Control. Release* **2001**, *73*, 121–136.

(6) Eloy, J. O.; Claro de Souza, M.; Petrilli, R.; Barcellos, J. P. A.; Lee, R. J.; Marchetti, J. M. *Colloids Surf. B. Biointerfaces* **2014**, *123C*, 345–363.

(7) Brown, M. T.; Bussell, J. K. *Mayo Clin. Proc.* **2011**, *86*, 304–314.

(8) Farokhzad, O. C.; Langer, R. *ACS Nano* **2009**, *3*, 16–20.

(9) Langer, R.; Peppas, N. A. *Biomaterials* **1981**, *2*, 201–214.

(10) Liechty, W. B.; Kryscio, D. R.; Slaughter, B. V; Peppas, N. A. *Annu. Rev. Chem. Biomol. Eng.* **2010**, *1*, 149–173.

(11) Whitehead, K. A.; Langer, R.; Anderson, D. G. *Nat. Rev. Drug Discov.* **2009**, *8*, 129–138.

(12) Hoare, T. R.; Kohane, D. S. *Polymer (Guildf).* **2008**, *49*, 1993–2007.

(13) Horcajada, P.; Chalati, T.; Serre, C.; Gillet, B.; Sebrie, C.; Baati, T.; Eubank, J. F.; Heurtaux, D.; Clayette, P.; Kreuz, C.; Chang, J.-S.; Hwang, Y. K.; Marsaud, V.; Bories, P.-N.; Cynober, L.; Gil, S.; Férey, G.; Couvreur, P.; Gref, R. *Nat. Mater.* **2010**, *9*, 172–178.

(14) Layre, A. M.; Gref, R.; Couvreur, P.; Richard, J. Nanoparticules polymériques composites. FR0407569, 2004.

(15) Hu, F.-Q.; Jiang, S.-P.; Du, Y.-Z.; Yuan, H.; Ye, Y.-Q.; Zeng, S. *Int. J. Pharm.* **2006**, *314*, 83–89.

(16) *Metal-Organic Frameworks: Applications from Catalysis to Gas Storage*; Farrusseng, D., Ed.; Wiley-VCH Verlag GmbH & Co. KGaA: Weinheim, Germany, 2011.

(17) Corma, A.; García, H.; Llabrés i Xamena, F. X. *Chem. Rev.* **2010**, *110*, 4606–4655.

(18) Ma, L.; Abney, C.; Lin, W. *Chem. Soc. Rev.* **2009**, *38*, 1248–1256.

(19) Yoon, M.; Srirambalaji, R.; Kim, K. *Chem. Rev.* **2012**, *112*, 1196–1231.

(20) Farha, O. K.; Yazaydın, A. Ö.; Eryazici, I.; Malliakas, C. D.; Hauser, B. G.; Kanatzidis, M. G.; Nguyen, S. T.; Snurr, R. Q.; Hupp, J. T. *Nat. Chem.* **2010**, *2*, 944–948.

(21) Li, B.; Wen, H.-M.; Zhou, W.; Chen, B. *J. Phys. Chem. Lett.* **2014**, *5*, 3468–3479.

(22) Ma, S.; Zhou, H.-C. *Chem. Commun.* **2010**, *46*, 44–53.

(23) Li, J.-R.; Sculley, J.; Zhou, H.-C. *Chem. Rev.* **2012**, *112*, 869–932.

(24) Custelcean, R.; Moyer, B. A. *Eur. J. Inorg. Chem.* **2007**, *2007*, 1321–1340.

(25) Fei, H.; Rogow, D. L.; Oliver, S. R. J. *J. Am. Chem. Soc.* **2010**, *132*, 7202–7209.

(26) Kreno, L. E.; Leong, K.; Farha, O. K.; Allendorf, M.; Van Duyne, R. P.; Hupp, J. T. *Chem. Rev.* **2012**, *112*, 1105–1125.

(27) Miller, S. E.; Teplensky, M. H.; Moghadam, P. Z.; Fairen-Jimenez, D. *Interface Focus* **2016**, *6*.

(28) Li, H.; Eddaoudi, M.; O'Keeffe, M.; Yaghi, O. M. **1999**, *402*, 276–279.

(29) Bernini, M. C.; Fairen-Jimenez, D.; Pasinetti, M.; Ramirez-Pastor, A. J.; Snurr, R. Q. *J. Mater. Chem. B* **2014**, *2*, 766–774.

(30) Horcajada, P.; Serre, C.; Vallet-Regí, M.; Sebban, M.; Taulelle, F.; Férey, G. *Angew. Chemie Int. Ed.* **2006**, *45*, 5974–5978.

(31) Xiao, B.; Wheatley, P. S.; Zhao, X.; Fletcher, A. J.; Fox, S.; Rossi, A. G.; Megson, I. L.; Bordiga, S.; Regli, L.; Thomas, K. M.; Morris, R. E. *J. Am. Chem. Soc.* **2007**, *129*, 1203–1209.

(32) Abánades Lázaro, I.; Haddad, S.; Sacca, S.; Orellana-Tavra, C.; Fairen-Jimenez, D.; Forgan, R. S. *Chem* **2017**, *2*, 561–578.

(33) He, C.; Lu, K.; Liu, D.; Lin, W. *J. Am. Chem. Soc.* **2014**, *136*, 5181–5184.

(34) Ruyra, À.; Yazdi, A.; Espín, J.; Carné-Sánchez, A.; Roher, N.; Lorenzo, J.; Imaz, I.; Maspoch, D. *Chem. - A Eur. J.* **2015**, *21*, 2508–2518.

(35) Tamames-Tabar, C.; Cunha, D.; Imbuluzqueta, E.; Ragon, F.; Serre, C.; Blanco-Prieto, M. J.; Horcajada, P. *J. Mater. Chem. B* **2014**, *2*, 262–271.

(36) Orellana-Tavra, C.; Baxter, E. F.; Tian, T.; Bennett, T. D.; Slater, N. K. H.; Cheetham, A. K.; Fairen-Jimenez, D. *Chem. Commun.* **2015**, *51*, 13878–13881.

(37) Orellana-Tavra, C.; Marshall, R. J.; Baxter, E. F.; Lázaro, I. A.; Tao, A.; Cheetham, A. K.;

Forgan, R. S.; Fairen-Jimenez, D. *J. Mater. Chem. B* **2016**, *4*, 7697–7707.

(38) Cavka, J. H.; Jakobsen, S.; Olsbye, U.; Guillou, N.; Lamberti, C.; Bordiga, S.; Lillerud, K. P. *J. Am. Chem. Soc.* **2008**, *130*, 13850–13851.

(39) Deria, P.; Bury, W.; Hupp, J. T.; Farha, O. K. *Chem. Commun.* **2014**, *50*, 1965–1968.

(40) Guillerm, V.; Ragon, F.; Dan-Hardi, M.; Devic, T.; Vishnuvarthan, M.; Campo, B.; Vimont, A.; Clet, G.; Yang, Q.; Maurin, G.; Férey, G.; Vittadini, A.; Gross, S.; Serre, C. *Angew. Chemie* **2012**, *124*, 9401–9405.

(41) Mondloch, J. E.; Bury, W.; Fairen-Jimenez, D.; Kwon, S.; DeMarco, E. J.; Weston, M. H.; Sarjeant, A. A.; Nguyen, S. T.; Stair, P. C.; Snurr, R. Q.; Farha, O. K.; Hupp, J. T. *J. Am. Chem. Soc.* **2013**, *135*, 10294–10297.

(42) Kung, C.-W.; Wang, T. C.; Mondloch, J. E.; Fairen-Jimenez, D.; Gardner, D. M.; Bury, W.; Klingsporn, J. M.; Barnes, J. C.; Van Duyne, R.; Stoddart, J. F.; Wasielewski, M. R.; Farha, O. K.; Hupp, J. T. *Chem. Mater.* **2013**, *25*, 5012–5017.

(43) Fu, Y.; Kao, W. J. *Expert Opin. Drug Deliv.* **2010**, *7*, 429–444.

(44) Ströhl, F.; Kaminski, C. F. *Methods Appl. Fluoresc.* **2015**, *3*.

(45) Ströhl, F.; Kaminski, C. F. *Optica* **2016**, *3*, 667–677.

(46) Young, L. J.; Ströhl, F.; Kaminski, C. F. *J. Vis. Exp.* **2016**.

(47) Chen, W.; Young, L. J.; Lu, M.; Zaccone, A.; Ströhl, F.; Yu, N.; Kaminski Schierle, G. S.; Kaminski, C. F. *Nano Lett.* **2017**, *17*, 143–149.

(48) Cunha, D.; Ben Yahia, M.; Hall, S.; Miller, S. R.; Chevreau, H.; Elkaïm, E.; Maurin, G.; Horcajada, P.; Serre, C. *Chem. Mater.* **2013**, *25*, 2767–2776.

(49) Fantham, M.; Kaminski, C. F. *Nat. Photonics* **2017**, *11*, 69–69.

(50) Mellman, I. *Annu. Rev. Cell Dev. Biol.* **1996**, *12*, 575–625.

(51) Rejman, J.; Oberle, V.; Zuhorn, I. S.; Hoekstra, D. *Biochem. J.* **2004**, *377*, 159–169.

(52) Mayor, S.; Pagano, R. E. *Nat. Rev. Mol. Cell Biol.* **2007**, *8*, 603–612.

(53) Orellana-Tavra, C.; Mercado, S. A.; Fairen-Jimenez, D. *Adv. Healthc. Mater.* **2016**, *5*, 2261–2270.

(54) Dutta, D.; Donaldson, J. G. *Cell. Logist.* **2012**, *2*, 203–208.

(55) Ivanov, A. I. 2008; pp. 15–33.

(56) dos Santos, T.; Varela, J.; Lynch, I.; Salvati, A.; Dawson, K. A. *PLoS One* **2011**, *6*, e24438.

(57) Sonveaux, P.; Végran, F.; Schroeder, T.; Wergin, M. C.; Verrax, J.; Rabbani, Z. N.; De

Saedeleer, C. J.; Kennedy, K. M.; Diepart, C.; Jordan, B. F.; Kelley, M. J.; Gallez, B.; Wahl, M. L.; Feron, O.; Dewhirst, M. W. *J. Clin. Invest.* **2008**, *118*, 3930–3942.

(58) Sonveaux, P.; Copetti, T.; De Saedeleer, C. J.; Végran, F.; Verrax, J.; Kennedy, K. M.; Moon, E. J.; Dhup, S.; Danhier, P.; Frérart, F.; Gallez, B.; Ribeiro, A.; Michiels, C.; Dewhirst, M. W.; Feron, O. *PLoS One* **2012**, *7*, e33418.

(59) Pérez-Escuredo, J.; Van Hée, V. F.; Sboarina, M.; Falces, J.; Payen, V. L.; Pellerin, L.; Sonveaux, P. *Biochim. Biophys. Acta* **2016**, *1863*, 2481–2497.

(60) Wang, T. C.; Vermeulen, N. A.; Soo Kim, I.; F Martinson, A. B.; Fraser Stoddart, J.; Hupp, J. T.; Farha, O. K. *Nat. Protoc.* **2015**, *11*, 149–162.

(61) Li, P.; Klet, R. C.; Moon, S.-Y.; Wang, T. C.; Deria, P.; Peters, A. W.; Klahr, B. M.; Park, H.-J.; Al-Juaid, S. S.; Hupp, J. T.; Farha, O. K. *Chem. Commun.* **2015**, *51*, 10925–10928.

Table of contents (TOC) graphic